13th International Symposium on Particle Image Velocimetry – ISPIV 2019
Munich, Germany, July 22-24, 2019

Simultaneous measurement of velocity and concentration fields in Hele-Shaw cell

Mobin Alipour[1,2], Marco De Paoli[1,*], Alfredo Soldati[1,2]

[1] Institute of Fluid Mechanics and Heat Transfer, TU Wien, 1060 Vienna, Austria

[2] Polytechnic Department, University of Udine, 33100 Udine, Italy

[*] marco.de.paoli@tuwien.ac.at

Abstract

While the wealth of computational studies has shed a light on some fundamental features of convective dissolution in porous media, experimental techniques currently adopted do not allow an easy, simultaneous and accurate measurement of concentration and velocity fields. With this work, we aim precisely at this gap. We performed experiments in Hele-Shaw cell and used an optical technique to obtain the solute concentration field. We propose a concentration-based velocity reconstruction (CVR) algorithm, i.e. a new method to reconstruct the velocity field from the solute concentration measurements. We compare the CVR results with the velocity fields obtained via particle tracking velocimetry (PTV) measurements, giving the guidelines for future experimental works.

1 Introduction

The process of convective dissolution in porous media is of fundamental importance in a number of industrial and geophysical applications (Liang et al., 2018). Recently, this problem received renovated attention due to the storage of carbon dioxide (CO2) in underground geological formations, which has been identified as a possible remedy to the greenhouse effect (Huppert and Neufeld, 2014). When liquefied CO2 is injected in deep saline aquifers, it dissolves with the surrounding fluid (brine) and remains safely stored (De Paoli et al., 2016). In this instance, it is of crucial importance to predict the time taken to dissolve a certain amount of CO2 and to determine the reliability of a potential sequestration site. This problem, usually modelled as a Rayleigh-Bénard configuration (De Paoli et al., 2017), has driven a number of numerical and experimental studies that aim at understanding the dissolution dynamics controlling the CO2 storage process (Riaz and Cinar, 2014). While numerical simulations can provide detailed information in terms of velocity and concentration fields in the limit of small domains, current experiments can give accurate concentration field measurements for larger domains, but no information about the fluid velocity. In this work, we aim at bridging this gap.

We investigate the process of convective dissolution in a saturated porous layer with the aid of a Hele-Shaw cell, consisting of two parallel and transparent plates separated by a narrow gap. An aqueous solution of potassium permanganate (KMnO4) and water are chosen as analogue fluids to mimic the behaviour of CO2+brine mixture and brine, respectively. We infer solute concentration field over the entire cell at high resolution and accuracy from transmitted light intensity (Slim et al., 2013). Moreover, we developed a concentration-based velocity reconstruction (CVR) method, which allows an accurate estimation of the velocity distribution and is solely based on the fields obtained from the concentration measurements. We applied the stream function formulation to the Darcy equation. The CVR method has been first validated with synthetic data obtained from numerical simulations and then compared with experimental velocity measurements achieved via particle tracking velocimetry (PTV).

The paper is organised as follows. In Sec. 2 we describe the experimental apparatus, with particular attention to the choice of the working fluids and the setup used for the PTV. In Sec. 3 we describe the CVR algorithm and we derive the boundary conditions for the present configuration. The algorithm validation and the comparison of the velocity field obtained with CVR and PTV is discussed in Sec. 4. Finally, in Sec. 5 we summarise the results and outline possible further improvements.

2 Methodology

2.1 Experimental setup

We investigate convective dissolution in one-sided porous media configuration (Hewitt et al., 2013; De Paoli et al., 2017), consisting of a rectangular domain initially filled with pure fluid only, i.e. $C(x,z,t=0)=0$, where C is the solute concentration and x,z and t are the spatial and temporal coordinates respectively. The domain boundaries are impermeable to fluid and solute, with the exception of the top boundary, along which the concentration is kept constant [$C(x,z=H,t)=C_s$, being C_s the saturation value]. We infer density fields at high resolution and accuracy from transmitted light intensity (Slim et al., 2013; Ching et al., 2017).

The archetypal one-sided configuration is obtained experimentally with the Hele-Shaw cell, consisting of two parallel acrylic plates (thickness 30 mm), with the length of $L=160$ mm and height $H=346$ mm, separated by a narrow gap $b=0.3$ mm. The apparatus is sketched in Fig. 1. The gap thickness b must be small enough to represent a pseudo two-dimensional flow (Fernandez et al., 2002; Slim et al., 2013; Oltean et al., 2008), described by a parabolic velocity profile (Ehyayi and Kiger, 2014). For low velocities, we have a Darcy-type flow and the domain is characterised by a uniform permeability $k=b^2/12$ (Zeng et al., 2003).

Except the top wall, all boundaries are confined by tailor-made rubber seals. The material used for the sealings is a high-quality impermeable rubber based on aramid fibre with nitrile binder (Klinger–sil C–4400), which are worked with high-precision CNC machines. Along the top wall lies a steel mesh (40 μm grid size) that contains the solute powder.

2.1.1 Working fluids

The behaviour of the CO2+brine mixture and brine is mimicked by an aqueous solution of potassium permanganate (KMnO4) and water. Viscosity and diffusion are assumed constant and equal to $\mu=9.2\times10^{-4}$ Pa·s and $D=1.65\times10^{-9}$ m^2/s respectively (Slim et al., 2013). The mixture's density ρ can be well approximated by a linear function of the solute concentration C:

$$\rho=\rho_s\left[1+\frac{\Delta\rho_s}{\rho_s C_s}\left(C-C_s\right)\right], \tag{1}$$

where ρ_s is the density of the saturated solution, $C_s=48$ kg/m^3 is the saturation value of concentration and $\Delta\rho_s$ is the density difference between saturated solution and pure water. Since water density is sensitive to temperature, ρ_s and $\Delta\rho_s$ are estimated in each experiment based on the correlations of Novotný and Söhnel (1988) . The variation of the mixture's density as a function of the KMnO4 concentration is shown in Fig. 2.

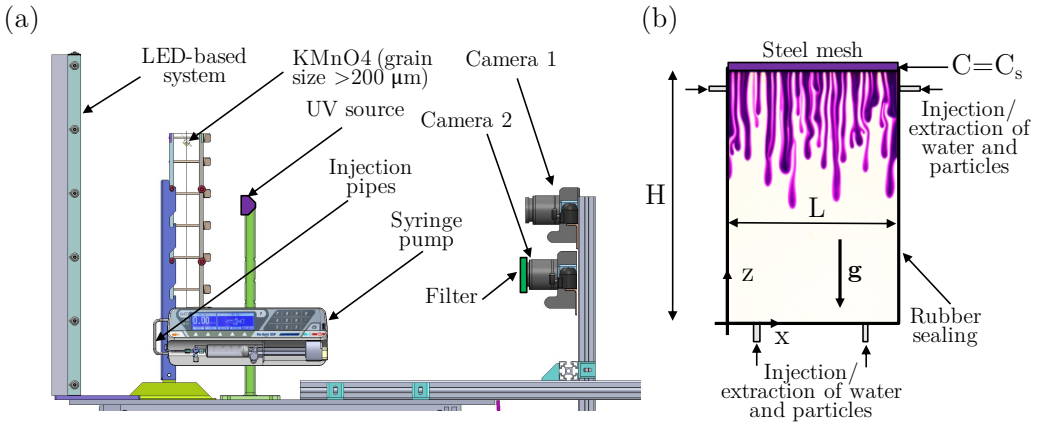

Figure 1: Experimental setup. (a) Side view of all main components of the apparatus. The cameras used for the concentration measurements and for the particle tracking, indicated with Camera 1 and Camera 2 respectively, are also shown. (b) Front view of the Hele-Shaw cell with an exemplar light intensity distribution (purple water-KMnO4 fingers are shown). The domain dimensions (L,H) are indicated. Along the steel mesh the dye is poured, and therefore the solute concentration is considered as constant.

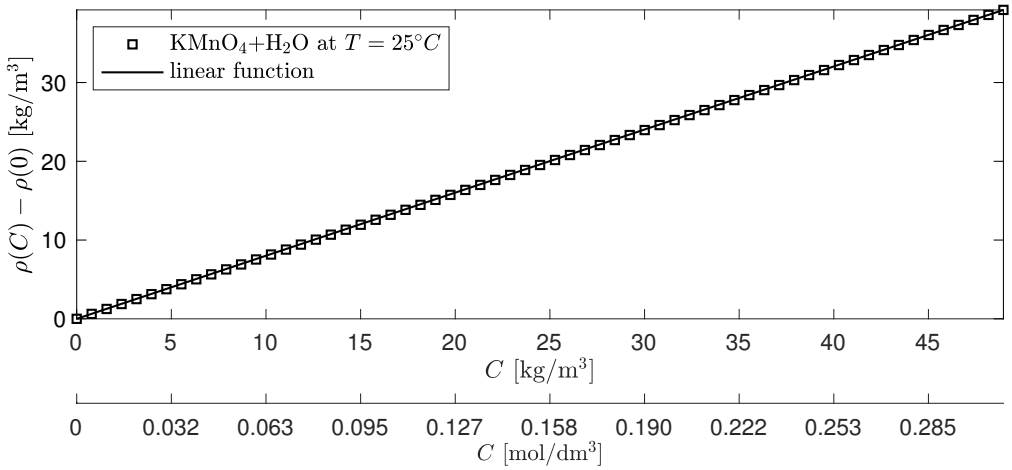

Figure 2: Variation of the fluid density as a function of the solute concentration. The density value obtained with the polynomial correlation by Novotný and Söhnel (1988) (symbols) is very well fitted by a linear function [Eq. (1), solid line]. The density profile is obtained at a constant temperature $T = 25°C$.

We have chosen these fluid also to make a comparison easier between experiments and simulations, since most of numerical studies assumed such a linear dependency (Riaz and Cinar, 2014).

Grains of potassium permanganate (grains size greater than 200 μm) are poured on top of the cell, where the grid is located. Afterwards, the light fluid (water) is injected with the aid of a syringe pump from two channels at the bottom of the cell, and the fluid level is increased up to the upper boundary. When the water level reaches the cell top, the pump is shut down. Solute dissolves in water and a fluid layer denser than water forms below the grid: After an initial diffusive phase, the layer of heavy mixture formed below the grid thickens and becomes unstable, and finger like structures form (De Paoli et al., 2017).

2.1.2 Calibration and reconstruction of the concentration field

The system requires a proper calibration for each value of the cell gap b and for each illumination condition, which can be summarised as follows. Many solution samples are prepared with the aid of a high-precision scale (Sartorius Acculab Atilon model ATL-423-I, $\pm 10^{-4}$ g), which allows a precise estimation of the solute mass fraction ω in the mixture. Then the evolution of the solute distribution is recorded with a Canon EOS 1300D camera (3456×5184 px), which is used to reconstruct the concentration field during the experiments (Camera 1 in Fig. 1). When this camera takes the pictures, the LED-based illumination system is turned on and the light intensity produced is uniformly distributed over the cell. During the calibration procedure, a picture of the entire domain is recorded, then the light intensity is averaged over the cell and the mean value is obtained. An example of calibration curve is shown in Fig. 3. It is of crucial importance to repeat the calibration in correspondence of each thickness adopted and it is also important to choose the value of the voltage applied to the light source to maximise the sensitivity of apparatus (Alipour and De Paoli, 2019).

The solute concentration distribution is reconstructed with the aid of an in-house MatLab code. The input data consist of the fluid temperature, measured with a thermometer ($\pm 0.1°C$) before injection in the cell, and the normalised light intensity distribution I (i.e. the light intensity divided by its maximum value) obtained from the camera. First, with the aid of the calibration curves, the solute mass fraction distribution is reconstructed over the entire image. The mass fraction is related to the solute concentration through the relationship $C(\omega) = \rho(\omega)\omega(I)$. Then the mixture's density, which is a function of the water's density (i.e. a function of temperature) and of the solute mass fraction, is obtained with empirical polynomial correlations (Novotný and Söhnel, 1988). Therefore, for a given temperature, it is possible to correlate the light intensity to the solute concentration.

2.2 Particle tracking velocimetry measurements

Ehyayi and Kiger (2014) measured the velocity field in a Hele-Shaw geometry with the aid of PIV technique and identified three possible regimes for the particles motion that are related to the position of the particle

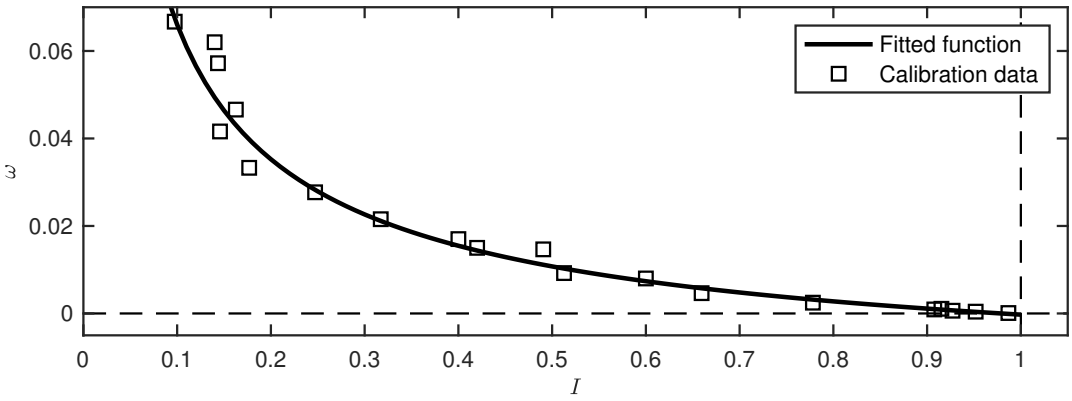

Figure 3: Calibration curve obtained. The solute mass fraction ω is shown as a function of the normalised light intensity I. The maximum intensity value ($I = 0$) corresponds to the minimum solute mass fraction ($\omega = 0$, pure water). The experimental measurements (symbols) are well fitted by a third-order polynomial (solid line).

in the in-plane direction, y. After a moving within the cell, particles will mainly stay on two planes symmetrically located at the same distance $0.2b$ from the side boundaries of the cells. Therefore, Ehyayi and Kiger (2014) observed that it is of fundamental importance that when particles are used as tracers, they are distributed along these two planes, i.e they are at the equilibrium. In this work, we will use this equilibrium condition in the present Hele-Shaw geometry. To achieve this state, we inject the particles-seeded water from two channels located at the bottom of the cell and, at the same time, we extract water from two channel located at upper side of the cell [see Fig. 1(b)]. We iterate this procedure in both directions inducing a pulsating flow in which viscous forces dominate over transient inertial forces, i.e. with a Womersley number Wo

$$Wo = \frac{b}{2}\sqrt{\frac{2\pi f}{\nu}} < 1 \, . \tag{2}$$

In this way, the parabolic profile within the gap is preserved (Ehyaei, 2014). We conclude that, with the exception of the area in the nearby of the injection/extraction points, the particles fulfil the equilibrium condition.

The particles used consist of fluorescent UV microspheres (density 980 kg/m^3, diameter 27-32 μm) that emit green light (525 nm peak) after UV excitation at 365 nm. Particles are illuminated by 4 UV-A lamps (each of power 4 W), reported in Fig. 1(a). Particles motion is recorded by a Canon EOS 77D camera (6000 $\times$ 4000 px) with 18-55 mm lenses at 3 fps. The camera, labelled as Camera 2 in Fig. 1(a), is equipped with a bandpass filter BP 540–80 HT (515 – 565 nm), so that the maximum sensitivity is obtained in correspondence of the wavelength of the light emitted from the particles. The images are binarised and the processed to reconstruct the velocity field.

3 Concentration-based velocity reconstruction (CVR)

The narrow gap thickness of the Hele-Shaw cell allows the flow to be pseudo two-dimensional and consequently the apparatus can reproduce a Darcy flow. Based on this simple assumption, we developed a concentration-based velocity reconstruction (CVR) method. We consider the flow in the gap as incompressible and we assume that the Boussinesq approximation can be applied. The velocity field is controlled by the continuity and the Darcy equations, respectively

$$\nabla \cdot \mathbf{u} = 0 \qquad , \qquad \mathbf{u} = -\frac{b^2}{12\mu}(\nabla p + \rho \mathbf{g}) \, , \tag{3}$$

where $\mathbf{u}$ is the Darcy velocity, p is the pressure and $\mathbf{g}$ is the acceleration due to gravity. We consider the fluid density as the only physical property that depends on concentration through the correlation (1).

The procedure of velocity reconstruction is based on the information available from the concentration measurements. We introduce the stream function (Batchelor, 1968, p. 78) defined as $(u, w) = (\partial_z \psi, -\partial_x \psi)$.

Taking the curl of Eq. (2) and assuming 2D flow ($u_y = \partial_y \cdot = 0$), we correlate the concentration gradient to the stream function via the Poisson equation:

$$\nabla^2 \psi = \alpha \frac{\partial C}{\partial x} , \tag{4}$$

being $\alpha = b^2 g \Delta\rho_s / (12 \mu C_s)$. The concentration derivative in Eq. (4) is obtained from the experimental measurements.

3.1 Boundary conditions and numerical solution

The problem, sketched in Fig. 4 with indication of the boundary conditions for the flow and the concentration fields, is now formulated in terms of the stream function $\psi(x,z)$. Eq. (4) is solved numerically with the boundary conditions determined as follows. Since along the top boundary the concentration is constant $[C(x, z = H) = Cs]$ and due to the no-penetration b.c. in z direction $[w(x, z = H) = 0]$, Eq. (4) and definition of ψ give:

$$\nabla^2 \psi(x, z = H) = 0 \qquad \text{and} \qquad \left. \frac{\partial \psi}{\partial x} \right|_{(x,z=H)} = 0 . \tag{5}$$

Across the left boundary there is no solute flux ($\partial_x C = 0$) and the normal component of velocity is zero ($u = 0$) and therefore, in terms of stream function we have:

$$\nabla^2 \psi(x = 0, z) = 0 \qquad \text{and} \qquad \left. \frac{\partial \psi}{\partial z} \right|_{(x=0,z)} = 0 , \tag{6}$$

and similarly for the right boundary ($x = L$). Finally, at the bottom boundary there is no penetration ($w = 0$), therefore:

$$\left. \frac{\partial \psi}{\partial x} \right|_{(x,z=0)} = 0 . \tag{7}$$

From Eqs. (5)-(7), we conclude that ψ is constant along the boundaries, and since the streamlines are impenetrable to fluid, all boundaries are characterised by the same streamline defined by the constant β, i.e. $\psi = \beta$, and we arbitrarily set $\beta = 0$ so that

$$\psi = 0 \text{ on all the boundaries.} \tag{8}$$

Eq. (4) is solved numerically with boundary conditions (8). We used a 6th order 9-points compact finite difference scheme (Nabavi et al., 2007). Velocity components and all the other spatial derivatives are calculated using a 6th order finite difference scheme.

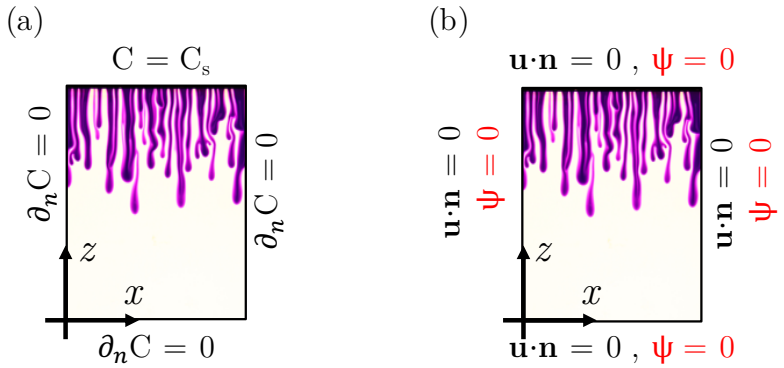

Figure 4: Boundary conditions for (a) concentration and (b) velocity and stream-function. In particular, $\psi = 0$ on the boundaries is assumed to solve Eq. (4), based on the experimental configuration adopted. The reference frame is also indicated.

4 Results

4.1 Algorithm validation with numerical results

The CVR algorithm is validated with data obtained from numerical simulations. The flow field $\mathbf{u}$ is incompressible and described by the Darcy law. Therefore it obeys the continuity and the Darcy equations (2). In absence of dispersion and assuming a constant diffusion coefficient, the solute concentration is controlled by the advection-diffusion equation

$$\frac{\partial C}{\partial t} + \mathbf{u} \cdot \nabla C = D \nabla^2 C. \tag{9}$$

We consider a rectangular domain (height $H = 50$ mm and length $L = 100$ mm). Since we want to validate the CVR algorithm in presence of Darcy flow, we assumed a very narrow gap ($b = 0.03$ mm) to estimate the permeability value used in the two dimensional simulation. However, a two-dimensional behaviour of the flow may be observed also for larger gap thicknesses (Letelier et al., 2019). We solve Eqs. (2) and (9) numerically in space using 2nd-order finite volumes and 6th-order compact finite differences schemes, respectively, in a uniform domain discretised with 400×200 nodes. Discretization in time is achieved using an explicit 3rd-order Runge-Kutta scheme. The code has been adapted from the original version used in previous works (Hidalgo et al., 2012, 2015). The boundary conditions, explicitly indicated in Fig. 4, are here summarised: concentration is fixed along the top boundary ($C = C_s$) and no-flux condition is assumed at the side and lower boundaries ($\partial_{\mathbf{n}} C = 0$). No-penetration is applied for the flow field along all the boundaries ($\mathbf{u} \cdot \mathbf{n} = 0$). The domain is initially saturated with pure water, i.e. $C(x, z < H, t = 0) = 0$, and characterised by a velocity $\mathbf{u} = (u, w) = 0$. The initial concentration field is perturbed so that, after the diffusion-dominated regime finger-like structures form and grow (De Paoli et al., 2017). An exemplar field is reported in Fig. 5(a), where the concentration contour map is shown together with the iso-contour lines.

Numerical data are used as follows: The horizontal concentration gradient in Eq. (4) is computed from the numerical concentration field $C(x, z)$. Following the algorithm described in Sec. 3, we obtain the stream function and reconstruct the velocity field. A qualitative comparison of the velocity fields obtained with numerical simulations and CVR is provided in Fig. 5(b)-(c), where a portion of the entire domain, indicated with the black rectangle in Fig. 5(a), is analysed. A more quantitative validation of the results obtained is given in Figs. 5(d)-(g). The horizontal (u) and vertical (w) velocities measured along the dashed line ($z = 25$) and the solid line ($z = 45$) in Fig. 5(a) are respectively shown in Figs. 5(d)-(e) and Figs. 5(f)-(g). Both qualitative and quantitative comparisons show an excellent agreement between CVR and numerical simulations.

4.2 Comparison of PTV and CVR results

We use the PTV velocity field to experimentally validate CVR algorithm. The experiment is performed for a time of approximately 10 minutes. The images, recorded at a frame rate of 1 fps for the CVR and 3 fps for the PTV, are stored and processed afterwards.

First, all the binarised images containing the particles are analysed to identify the particles that do not move during the experiment. The velocity field is then reconstructed with the PTV algorithm: The Lagrangian velocity distribution initially obtained from the particle tracking is interpolated on an Eulerian grid. The experimental concentration field [Fig. 6(a)] is used as input for the CVR algorithm. The stream function is computed and finally the velocity distribution is reconstructed. The velocity field is then averaged on a coarser grid, so that it matches the Eulerian grid obtained in the PTV case. A qualitative comparison of the results is provided in Fig. 6(b)-(c). The flow field $\mathbf{u}$ obtained with the CVR (red arrows) is in good agreement with the PTV velocity field (blue arrows).

From Fig. 6(b), we observe that in the nearby of the plume's interface no vector is present. This means that those regions are characterised either by a very low velocity or by a lack of data. We are in the second situation: The light emitted from the particles is absorbed by the solute-rich fluid and the particles are not visible. Therefore, for the experimental validation of the CVR with the PTV, we rely on the regions with low solute concentration. The horizontal and vertical velocities taken at $z = 142$ mm [dashed line in Fig. 6(a)], are compared in panels (d)-(e). PTV results (symbols) are reported on the Eulerian grid, whereas the reconstructed CVR velocities (dashed lines) are displayed with an error bar, corresponding to the values obtained assuming an approximation of $\pm 50\mu$m for the gap thickness. The x direction is classified in two regions: The white areas, corresponding to the low solute concentration ($x < 18$ mm, $x > 46$ mm), and the shaded areas, where the fingers are present and the concentration is higher (18 mm $< x <$ 33 mm, 38 mm $< x <$ 46 mm). Since for the reasons mentioned above the accuracy of the PTV in the present

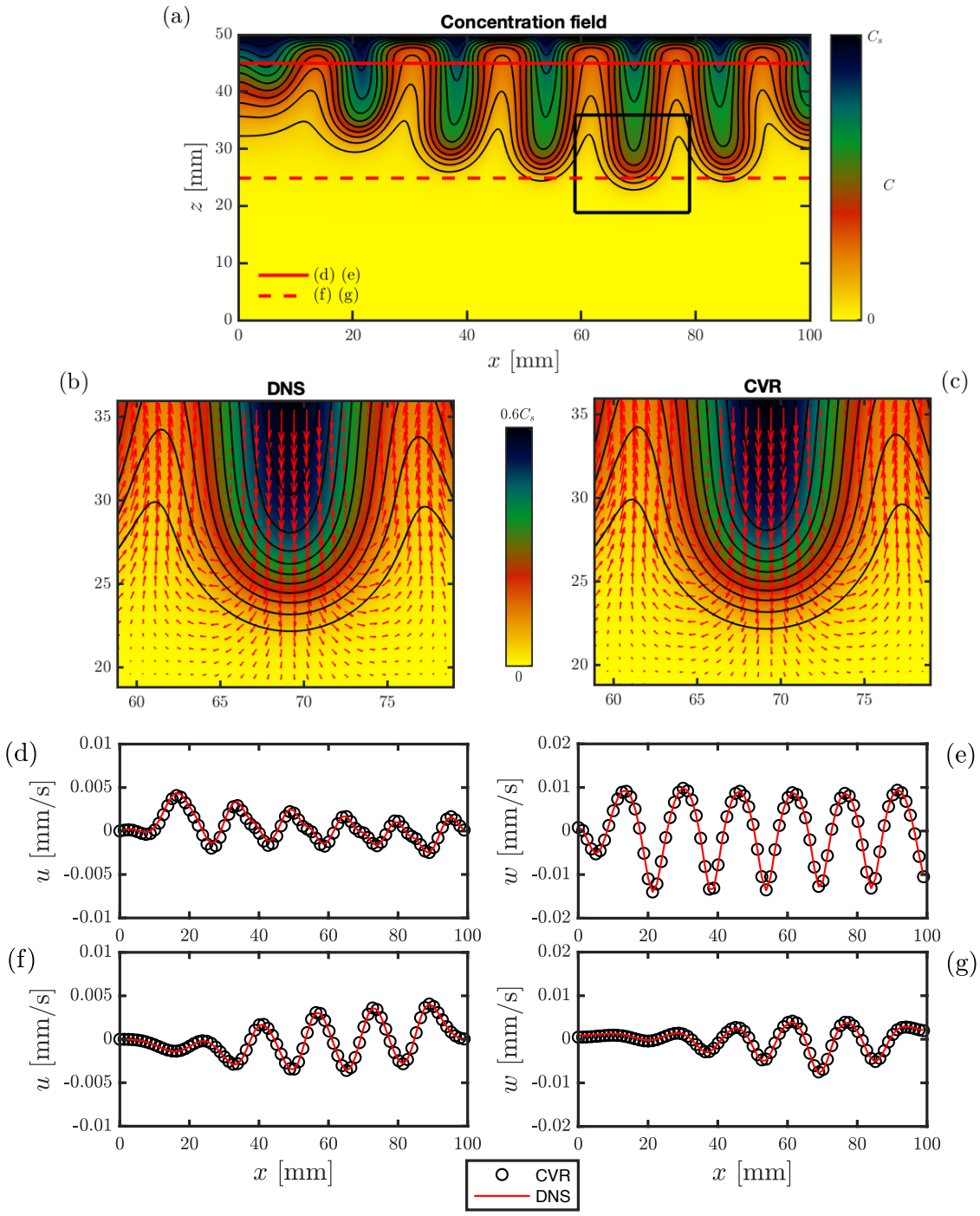

Figure 5: CVR algorithm validation. (a) Contour map of the concentration distribution obtained from the numerical simulation. The iso-contours of concentration (black lines) are also shown. A small portion of the domain, indicated with the black rectangle, is considered in panels (b)-(c). Detail of the velocity field (red vectors) obtained with numerical simulations (b) and with the CVR algorithm (c). The horizontal and vertical velocities measured along the two horizontal lines in panel (a) are reported in panels (d)-(g): Panels (d)-(e) measured at $z = 25$ mm (dashed line) and panels (f)-(g) $z = 45$ mm (solid line). The CVR results (symbols) are in excellent agreement with the numerical data (solid lines).

configuration is low inside the fingers, we consider only the low-concentration regions for the validation of the CVR algorithm, where PTV and CVR results are in good agreement. It is worth nothing that some differences occur in the region between the two fingers, i.e. for 33 mm $< x <$ 38 mm, probably due to both large solute concentration and lack of data. We conclude that the CVR algorithm is in good agreement with the experimental velocity measurements, which can be further improved by increasing the number particle per pixel.

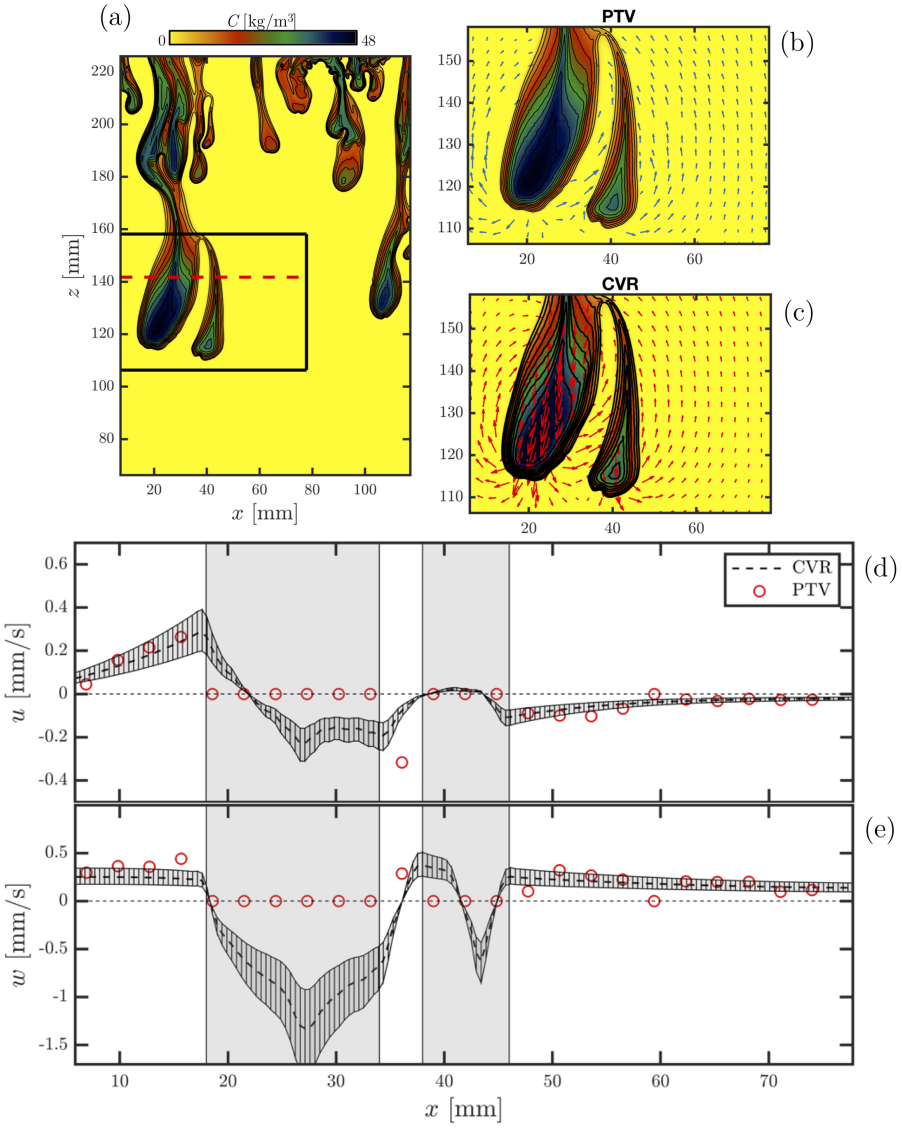

Figure 6: Comparison of PTV and CVR results. (a) Experimental concentration field (contour map and iso-contour lines). A detailed analyses of the region identified by the black rectangle is proposed in panels (b)-(c), where the velocity field is shown for PTV and CVR respectively. Comparison of the horizontal (d) and vertical (e) velocity fields measured along $z = 142$ mm [dashed line in panel (a)] show a good agreement of PTV and CVR results. The comparison should be considered within the region characterised by a low solute concentration (white areas) and not in the region occupied by the fingers (shaded areas).

5 Conclusions

We proposed a new method for the simultaneous measurement of solute concentration and velocity fields in Hele-Shaw cells. The algorithm proposed can be applied to Darcy flows, i.e. flows characterised by low Reynolds number and small gap thicknesses (Letelier et al., 2019). The algorithm has been validated first with numerical simulation data and then with particle tracking velocimetry measurements. The algorithm is characterised by high accuracy and easy implementation, which make this technique a good candidate for simultaneous velocity and concentration measurements in Hele-Shaw geometries.

With respect to PTV, this method has the advantage of providing accurate and high-resolved flow fields. Moreover, the velocity field can be also obtained in the dark regions of the flow, where the solute concentration is high and tracked particles might be not visible. The limited cost and complexity, the absence of laser sources and the presence of one single camera represent a further advantage for CVR method, that with a single picture allows a detailed reconstruction of the solute concentration and velocity fields. An example is shown in Fig. 7, where the input data consisting of a high-resolution picture (a), concentration field (b), flow streamlines (b), horizontal (c) and vertical (d) velocity distributions are shown.

A limitation of the current approach consists in the type of flow that can be described. When the flow is three-dimensional or characterised by dispersion, the Darcy law does not provide a good description of the flow field. Therefore, a possible improvement to the CVR method presented, which would make this approach reliable for a wider range of flow parameters, consists of the introduction of the dispersion effects (for a detailed analysis of the effect of mechanical dispersion in convective dissolution, see Liang et al., 2018; Letelier et al., 2019).

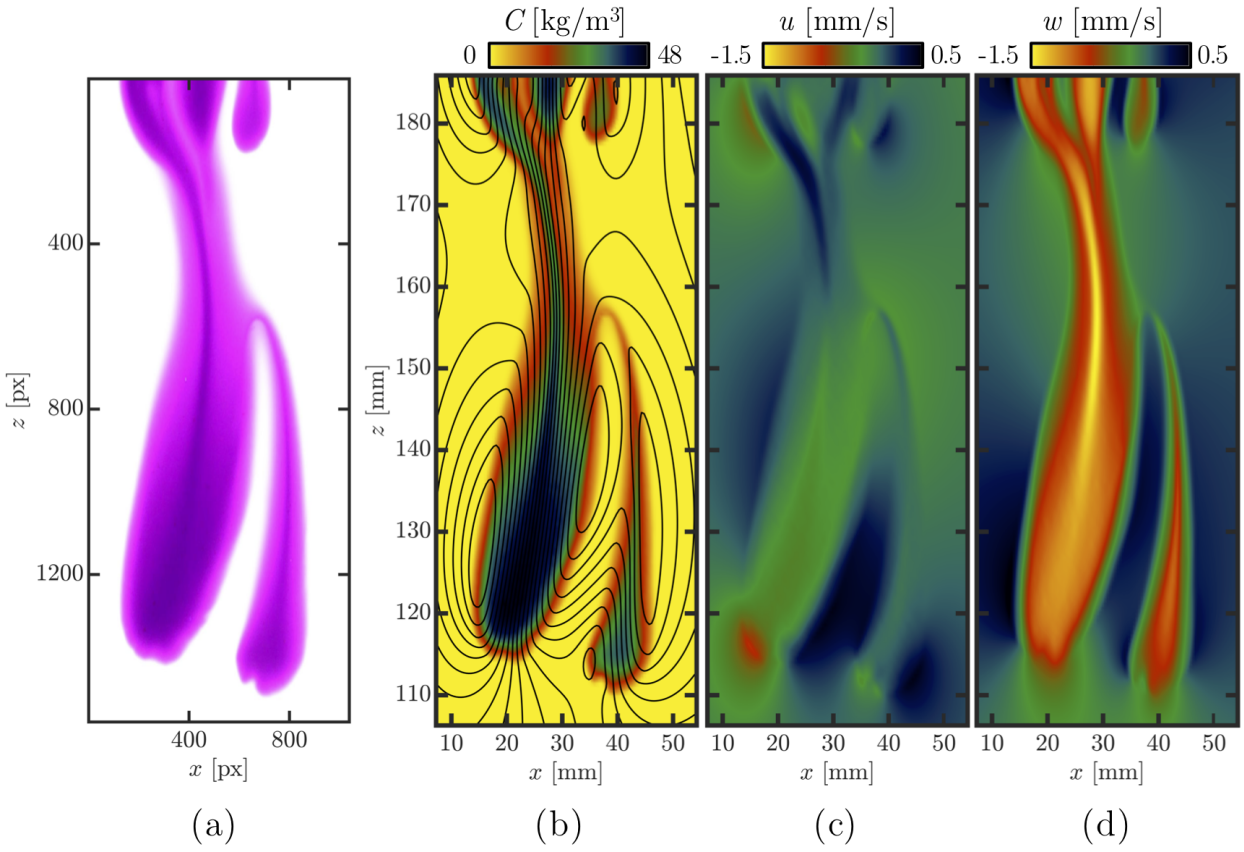

Figure 7: Process of concentration-based velocity reconstruction. (a) Experimental high-resolution image. The fluid is characterised by a purple colour, typical of the solute used. (b) Contour map of the concentration field (obtained from light intensities) and streamlines (reconstructed via CVR). (c)-(d) Horizontal and vertical velocity components, obtained from stream function formulation.

References

Alipour M and De Paoli M (2019) Convective dissolution in porous media: Experimental investigation in Hele-Shaw cell. *PAMM (accepted)* 19:–

Batchelor GK (1968) *An Introduction to Fluid Dynamics*. Cambridge University Press

Ching J, Chen P, and Tsai PA (2017) Convective mixing in homogeneous porous media flow. *Phys Rev Fluids* 2:014102

De Paoli M, Zonta F, and Soldati A (2016) Influence of anisotropic permeability on convection in porous media: implications for geological CO2 sequestration. *Phys Fluids* 28:056601

De Paoli M, Zonta F, and Soldati A (2017) Dissolution in anisotropic porous media: Modelling convection regimes from onset to shutdown. *Phys Fluids* 29:026601

Ehyaei D (2014) *An experimental investigation on solute natural convection in a vertical Hele-Shaw cell*. Ph.D. thesis. University of Maryland, College Park, Department of Mechanical Engineering

Ehyayi D and Kiger KT (2014) Quantitative velocity measurment in thin-gap Poiseuille flows. *Exp Fluids* 55:1706

Fernandez J, Kurowski P, Petitjeans P, and Meiburg E (2002) Density-driven unstable flows of miscible fluids in a Hele-Shaw cell. *J Fluid Mech* 451:239–260

Hewitt DR, Neufeld JA, and Lister JR (2013) Convective shutdown in a porous medium at high Rayleigh number. *J Fluid Mech* 719:551–586

Hidalgo JJ, Dentz M, Cabeza Y, and Carrera J (2015) Dissolution patterns and mixing dynamics in unstable reactive flow. *Geophys Res Lett* 42:6357–6364

Hidalgo JJ, Fe J, Cueto-Felgueroso L, and Juanes R (2012) Scaling of convective mixing in porous media. *Phys Rev Lett* 109:264503

Huppert HE and Neufeld JA (2014) The fluid mechanics of carbon dioxide sequestration. *Annual Review of Fluid Mechanics* 46:255–272

Letelier JA, Mujica N, and Ortega JH (2019) Perturbative corrections for the scaling of heat transport in a Hele-Shaw geometry and its application to geological vertical fractures. *J Fluid Mech* 864:746–767

Liang Y, Wen B, Hesse MA, and DiCarlo D (2018) Effect of dispersion on solutal convection in porous media. *Geophys Res Lett* 45:9690–9698

Nabavi M, Siddiqui MK, and Dargahi J (2007) A new 9-point sixth-order accurate compact finite-difference method for the helmholtz equation. *J Sound Vib* 307:972 – 982

Novotný P and Söhnel O (1988) Densities of Binary Aqueous Solutions of 306 Inorganic Substances. *J Chem Eng Data* 33:49–55

Oltean C, Golfier F, and Bue MA (2008) Experimental and numerical study of the validity of Hele-Shaw cell as analogue model for variable-density flow in homogeneous porous media. *Adv Water Resour* 31:82–95

Riaz A and Cinar Y (2014) Carbon dioxide sequestration in saline formations: Part I–Review of the modeling of solubility trapping. *J Petrol Sci Eng* 124:367–380

Slim AC, Bandi MM, Miller JC, and Mahadevan L (2013) Dissolution-driven convection in a Hele–Shaw cell. *Phys Fluids* 25:024101

Zeng J, Yortsos YC, and Salin D (2003) On the Brinkman correction in unidirectional Hele-Shaw flows. *Phys Fluids* 15:3829–3836